

Evaluation of Temporal and Spatial Characteristics of 2D HYPR Processing Using Simulations

Yan Wu,¹ Oliver Wieben,² Charles A. Mistretta,^{2,3} and Frank R. Korosec^{2,3*}

Highly constrained back-projection (HYPR) is a data acquisition and reconstruction method that provides very rapid frame update rates and very high spatial resolution for a time series of images while maintaining a good signal-to-noise ratio and high image quality. In this study we used simulations to evaluate the temporal and spatial characteristics of images produced using the HYPR algorithm. The simulations demonstrate that spatial accuracy is well maintained in the images and the temporal changes in signal intensity are represented with high fidelity. The waveforms representing signal intensity as a function of time obtained from regions-of-interest placed in simulated objects track the true curves very well, with variations from the truth occurring only when objects with very different temporal behavior are very close to each other. However, even when objects with different temporal characteristics are touching, their influences on each other are small. Magn Reson Med 59: 1090–1098, 2008. © 2008 Wiley-Liss, Inc.

Key words: HYPR; rapid imaging; time-resolved imaging; radial acquisition

There has been much work directed at improving temporal resolution in MRI. In one category of acceleration methods, only subsections of k -space data are acquired at each time interval, and the missing data are filled in by sharing or interpolating data from other time intervals. Examples include sliding-window reconstruction used with rectilinear (1), spiral (2), and radial (3) trajectories, as well as BRISK (4), Keyhole (5), and TRICKs (6). These methods provide rapid update rates, but the temporal window width of each timeframe can be large for some or all of the spatial frequency information, leading to a temporal latency for some of the information in the images.

In another category of acceleration methods, k -space trajectories are undersampled. Undersampled radial acquisition has been used to provide improved temporal resolution, where large undersampling factors have been used to produce high temporal resolution images containing few streak artifacts and well-preserved spatial resolution. This strategy has been used with a 3D stack-of-stars trajectory (7), in combination with TRICKs (8,9), and with the VIPR trajectory (10).

Acceleration has been achieved using parallel imaging methods, such as SMASH (11), SENSE (12), and GRAPPA

(13), which make effective use of information from multielement receiver coils to reduce the amount of data necessary to achieve a given spatial resolution. Other recently developed techniques such as k -t BLAST (14) and the biplane projection method (15) take advantage of the redundancy of spatial information that is normally inherent in a conventional time series.

More recently, the HYPR processing method (16) has been developed, which allows very large increases in the frame update rate of time-resolved scans. In this method, similar to that of the RIGR method (17), the spatial information comes from a nearly fully sampled, high spatial resolution, high-quality reference image, and the temporal information comes from a more sparsely sampled temporal weighting image. With HYPR data are acquired as a series of interleaves, each consisting of a unique subset of radial k -space sample lines. Each interleaf is used to produce a highly undersampled temporal weighting image. Additionally, multiple interleaves are combined to produce a fully sampled or nearly fully sampled dataset that is used to produce a high-quality composite image to reveal the spatial distribution of objects. Multiplication of temporal weighting images by spatial-reference composite images yields a series of high signal-to-noise ratio (SNR), low-artifact images, with good spatial and temporal resolution.

The aim of this study was to use computer simulations to evaluate the ability of the HYPR reconstruction method to accurately represent objects both spatially and temporally. The spatial and temporal accuracy of the HYPR images was studied as a function of the number of projections per composite image and per temporal weighting image for a variety of spatial and temporal conditions. Spatial considerations included object sizes, shapes, and spacing, and temporal considerations included the shape of the signal-intensity-versus-time waveforms as well as the diversity of the waveforms among different objects in the same image. The results of this study were used to aid in the proper selection of acquisition and reconstruction parameters for different clinical applications.

MATERIALS AND METHODS

To evaluate the properties of HYPR, computer simulations were performed using MatLab (MathWorks, Natick, MA). A series of 2D input images was produced for each simulation. One or more objects were generated in each image. Within each object the signal intensities of all pixels changed in the same manner. The signal intensity of each object was made to vary in time according to a linear, sine, or gamma-variate function to simulate temporal changes in signal intensity that might be observed clinically, such as when imaging the passage of contrast material through arteries and veins during an MR angiography (MRA) pro-

¹Department of Electrical and Computer Engineering, University of Wisconsin, Madison, Wisconsin.

²Department of Medical Physics, University of Wisconsin, Madison, Wisconsin.

³Department of Radiology, University of Wisconsin, Madison, Wisconsin.

*Correspondence to: Frank R. Korosec, PhD, University of Wisconsin Hospital and Clinics, 600 Highland Ave., Madison, WI 53792-1590. E-mail: FKorosec@uwhealth.org

Received 30 April 2007; revised 14 November 2007; accepted 27 December 2007.

DOI 10.1002/mrm.21564

Published online in Wiley InterScience (www.interscience.wiley.com).

© 2008 Wiley-Liss, Inc.

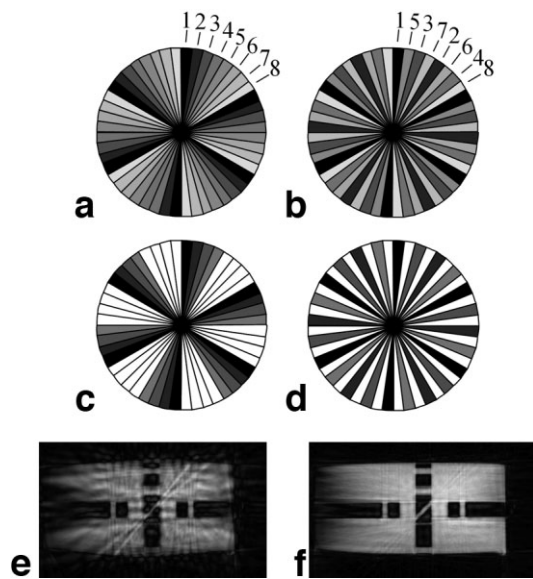


FIG. 1. Different acquisition orders for interleaved sets of projections used with HYPR processing: (a) sequential order, full dataset, (b) bit-reversed order, full dataset, (c) sequential order, partial dataset, (d) bit-reversed order, partial dataset, (e) an image reconstructed using data arranged similar to that shown in (c) where far less than a full set of projections was used, and (f) an image reconstructed using data arranged similar to that shown in (d), where again, far less than a full set of projections was used. The acquisition order is from dark to light (black to light gray), white represents missing data. Data were acquired as interleaved sets of profiles: black in the first interleaf, dark gray in the second, lighter gray in the third, etc., in order of decreasing shades of gray.

cedure, which is of particular interest in this study. The input images were sampled using a Radon transform, which produced profiles of the simulated images at various projection angles. (In MRI, equivalent profile information can be obtained by sampling k -space along radial lines and Fourier transforming the sampled data.) Once profiles were obtained images were produced using the HYPR algorithm and the standard filtered back-projection algorithm for comparison.

In simulated input images most objects were circular or rectangular to represent blood vessels intersecting or lying in an image plane. The signal intensity within each circular object was set so that it was maximal at the center and decreased quadratically with radius, reaching a value of zero at the edge of the simulated object. Zero-mean Gaussian noise was added to each input image. Each simulated image contained 256×256 pixels.

The input images were sampled using interleaved sets of projections. Each interleaf consisted of projections evenly distributed around the unit circle (equal angular spacing). An angular offset between each interleaf was chosen so that when the entire set of interleaves was considered the angular spacing of all projections was equal. The sampling order of the sequence of interleaves was important. A bit-reversed sampling order was used. To establish the acquisition order the starting projection angle (that determined the angular offset) for each interleaf was sequentially numbered. The numbers were converted to binary,

the bit order of the binary numbers was reversed, and thus a new bit-reversed numbering series was formed. This series dictated the order in which the sequence of interleaves was sampled. With this method, the projection angles sampled during each subsequent interleaf filled in the largest remaining gap in the set of projection angles to be sampled. As demonstrated in Fig. 1b for an eight interleaf scan, the projections were sampled at angles 1, 9, 17, 25, ... for interleaf one, angles 5, 13, 21, 29, ... for interleaf two, angles 3, 11, 19, 27, ... for interleaf three, etc. (rather than sampling the set of interleaves sequentially at angles 1, 9, 17, 25, ... for interleaf one, angles 2, 10, 18, 26, ... for interleaf two, angles 3, 11, 19, 27, ... for interleaf three, etc. as shown in Fig. 1a). Notice that within an interleaf the projection angles are still sampled in a sequentially rotating order. A more global order that ignores interleaves and instead orders each individual projection to ensure it fills in the largest gap will be described in the Discussion section. An alternative acquisition order, referred to as the Golden Ratio order (18), has recently been developed to achieve a similar goal.

During HYPR reconstructions the composite images were formed using a standard filtered back-projection algorithm applied to all of the acquired data (all-inclusive composite) or a subset of the data centered at the current timeframe (sliding-window composite). The number of timeframes spanned by a composite image dictated the composite window width. The weighting images were produced by applying a nonstandard, unfiltered back-projection algorithm to data acquired in the current timeframe, which typically included as few as 8 to 16 profiles. The data were unfiltered in order to avoid intraobject signal cancellation caused by applying filtered back-projection to an incomplete set of profiles. In the final step of the HYPR reconstruction each weighting image was multiplied by the appropriate composite image.

A description of the HYPR processing algorithm can be written as follows:

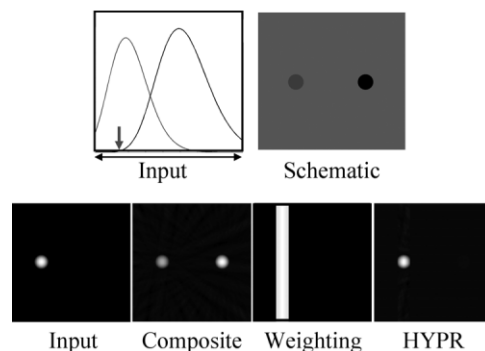


FIG. 2. When multiple objects appear in an image, as long as they do not overlap with each other in the projection direction, then a weighting image constructed using a single profile is sufficient to temporally weight a spatially accurate composite image. The left object in the schematic image changed intensity according to the early enhancing gamma-variate curve, and the right object in the schematic image changed intensity according to the late enhancing gamma-variate curve. The curves labeled as “input” were measured from the input time series of images and the curves labeled as “HYPR” were measured from the time series of images produced using the HYPR method.

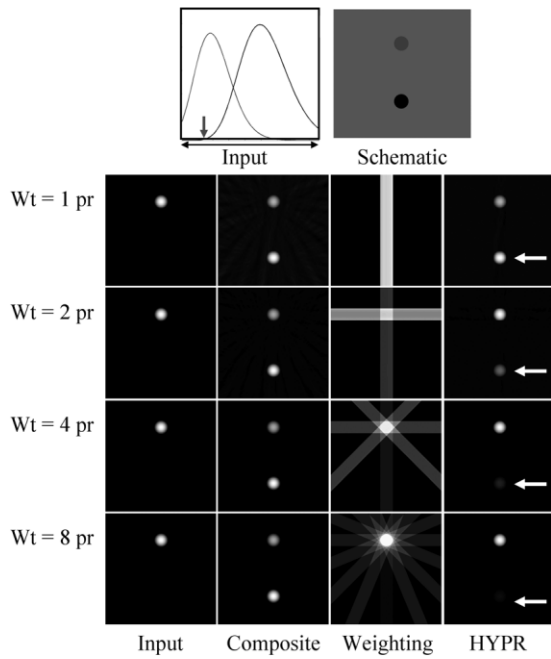


FIG. 3. If two or more objects overlap in the projection direction of a profile, then a weighting image constructed using that single profile is not sufficient to temporally weight a spatially accurate composite image. When this occurs, increasing the number of profiles used to construct the weighting image improves the accuracy of the HYPR images. In this simulation, the top object in the schematic changed intensity according to the early enhancing gamma-variate curve, and the bottom object in the schematic changed intensity according to the late enhancing gamma-variate curve. In this example, increasing the number of profiles (pr) to 2, 4, and 8 increasingly reduces the appearance of the inappropriately weighted object in the lower part of the image (arrows).

$$HYPR(x,y,t) = \frac{1}{n} \sum_{\theta=1}^n \frac{P_t(\rho,\theta,t)}{P_{comp}(\rho,\theta,t)} Comp(x,y,t) = W(x,y,t) \times Comp(x,y,t) \quad [1]$$

where, for a given timeframe t , $HYPR$ is a HYPR image, $Comp$ is a composite image formed by applying a standard filtered back projection algorithm to a large set of data composed of several consecutive frames, P_t is a projection acquired at angle θ , P_{comp} is a corresponding projection produced at angle θ using data from the composite image, and n is the number of projections used to produce each weighting image. The weighting images W are formed by backprojecting subsets ($\theta = 1$ to n) of unfiltered, normalized data. In order to prevent $P_t(\rho,\theta,t) / P_{comp}(\rho,\theta,t)$ from going to infinity as $P_{comp}(\rho,\theta,t)$ approached zero, all values of $P_{comp}(\rho,\theta,t)$ between 0 and a threshold value are set to the threshold value. The threshold value was chosen to be 5% of the maximum value of all the points along all profiles $P_{comp}(\rho,\theta,t)$ for a given weighting image ($\theta = 1$ to n).

HYPR results were assessed by qualitatively and quantitatively comparing the series of output images to the series of input images. To quantify the accuracy of the signal in an individual HYPR image the discrepancy be-

tween the signal in a HYPR image and the signal in the input image was calculated as:

$$D(t) = \sqrt{\frac{\sum_{(x,y)} (HYPR(x,y,t) - Input(x,y,t))^2}{\sum_{(x,y)} Input(x,y,t)^2}}, \quad [2]$$

To quantify the temporal accuracy of the series of HYPR images, the temporal waveforms measured from the HYPR images (or from particular objects in the HYPR images) were compared to the temporal waveforms measured from the input images (or the same objects in the input images) and the cross-correlation between the curves was calculated.

In addition, the SNR for the HYPR images was assessed. The signal for a given object was measured as the mean intensity of all pixels within the object. The noise was measured as the standard deviation of intensities of all pixels within a large ROI outside of the object. The SNR was calculated as the ratio of these two values.

RESULTS

In the simulation shown in Fig. 2 the signal intensities of two objects varied according to gamma-variate functions. The circular object on the left enhanced early and the circular object on the right enhanced late. Input, weighting, composite, and HYPR images are shown for frame 13 (of 100), corresponding to the time immediately preceding enhancement of the late-enhancing object as demonstrated by the arrow in the graph showing the intensity-versus-time curves as measured from the input images. The objects were 32 pixels in diameter and were spaced four diameters between centers. It is demonstrated that when the two objects do not overlap in the projection direction, a weighting image produced using a single profile is sufficient to accurately represent the enhancement of the objects, even though the all-inclusive composite image

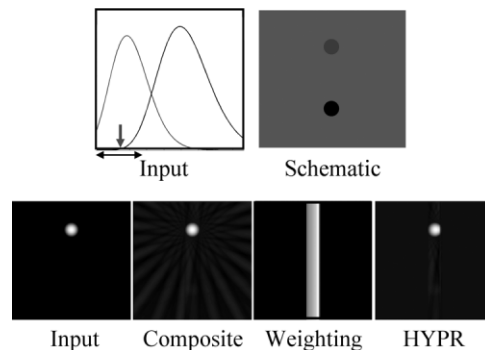


FIG. 4. Decreasing the composite window width (as indicated by the arrow spanning a fraction of the waveform plot) reduces the temporal averaging in the composite image, which is an effective means of preventing late-enhancing objects from appearing in the composite images used to produce the early timeframes in the HYPR series. This permits the use of fewer profiles in the weighting image while maintaining accuracy in the HYPR images. Compare this result to that shown in the first row of Fig. 3.

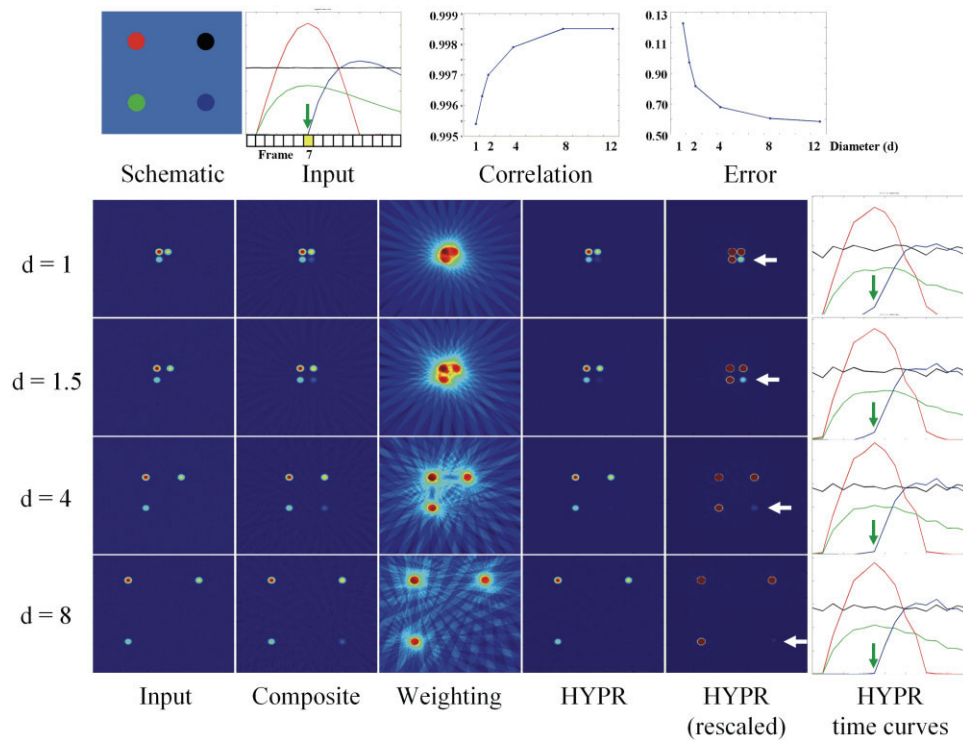


FIG. 5. The accuracy of the HYPR images decreased slightly as the objects were spaced closer together. This is due to the spatial imprecision inherent in the weighting image and the temporal averaging inherent in the composite image. Multiplication of the two images leads to improper temporal weighting of nearby objects as the temporal weighting meant for one object overlaps that for another object. In the rescaled HYPR images of this representation of timeframe 7 (green arrow in time curves), it can be seen that the object that should have zero signal (white arrows in rescaled HYPR images) is assigned increasingly higher signal when the objects are more closely spaced because the information in the weighting image is allowed to overlap this object by increasing amounts. For this object the cross-correlation between the curves measured from the input and HYPR images decreases as the spacing decreases. The absolute error between the input and HYPR images at timeframe 7 is shown to increase as the spacing decreases.

(constructed using all 100 profiles acquired throughout the entire acquisition, as demonstrated by the arrow spanning the duration of the signal intensity curves) represents a time-averaged signal from both of the objects.

For the simulation shown in Fig. 3 the signal intensity curves and the spatial configuration of the objects are the same as in the previous example, only the orientation of the objects relative to the initial projection angle is changed so that the two objects overlap in the single projection shown in the first row of images. If the temporal variations in the signal intensities of the two objects are not the same, then using that single profile (1 pr) to construct the weighting image (wt) is not sufficient to accurately represent the situation. In this case the late- and early-enhancing objects both appear in the HYPR image, despite that fact that only the early-enhancing object should appear in this early timeframe.

The final three rows in Fig. 3 show a comparison of images reconstructed using increasing numbers of projections per timeframe (weighting image, wt, formed using 2, 4, and 8 projections, pr). The input images are the same as those used for the simulation shown in the first row. This simulation demonstrates that increasing the number of projections in the weighting image leads to improvements in temporal accuracy, which is manifested in this case by a reduction in the signal from the late-enhancing object (arrows) that should not appear in this timeframe.

The simulation in Fig. 4 demonstrates the improvements in temporal accuracy obtained by using a sliding-window composite image. As in Fig. 3, a single profile was used in the weighting image. However, in this case only 25 profiles were used to produce a sliding-window composite image as demonstrated by the arrow that spans only a fraction of the duration of the signal intensity curves. Using fewer profiles to construct the composite image reduced the amount of temporal averaging of signal in this image. Therefore, much less signal from the late-enhancing object appeared in the composite image, allowing achievement of relatively accurate results using a weighting image constructed using only a single profile.

Figure 5 shows images from a single timeframe in which four objects (16 pixels in diameter) are spaced at 1, 1.5, 4, and 8 diameters between centers. Noise was added to the input images such that the peak SNR in the series was 40. Sixteen profiles were used to construct each timeframe and the composite window width was 5 out of 20 timeframes. The input signal intensity curves for the four objects are shown at the top of the figure. It is observed that the blurred (unfiltered back-projected) weighting information from the different objects begins to overlap as the spacing between objects decreases, leading to misrepresentation of the temporal characteristics in the HYPR images, as demonstrated by the increased distortion in the temporal waveforms between the input and HYPR curves

for each of the objects. For the latest-enhancing object (lower right in the schematic and images), the cross-correlation between the curves determined from the input and HYPR images was calculated as a function of the spacing between objects (as demonstrated by the graph labeled “correlation”). The cross-correlations were high, indicating good temporal agreement between HYPR and the truth. As the spacing decreased the cross-correlation between the signal intensity curves decreased, demonstrating less agreement between HYPR and the truth. For timeframe 7 shown in this figure, the absolute error between the input and HYPR images is shown to increase as the spacing decreases (as demonstrated by the graph labeled “error”). This is a general trend that occurred for the other objects and other timeframes in this and other similar simulations.

The simulation in Fig. 6 demonstrates a situation where a small object, with rapidly changing signal intensity, is completely surrounded by a larger object, with slowly increasing signal intensity. The diameters of the outer and inner objects are 64 and 16 pixels, respectively. Noise was added to the input images such that the peak SNR in the series was 40. Sixteen profiles were used to construct each timeframe, and the composite window width was 5 out of 20 timeframes. This arrangement represents a worst-case scenario for HYPR because the objects touch each other (so the inherent blur in the weighting image is detrimental), the outer object completely surrounds the inner object (so the signals from both objects overlap in every profile, resulting in inaccuracies in the signals in the weighting images), and the temporal characteristics of the two objects are dramatically different (so inaccuracies caused by the two effects mentioned above have great impact). Under these conditions the temporal waveforms measured from the HYPR series in this simulation show that the signal from the outer annular region is inappropriately enhanced when the signal in the inner circle enhances, and the signal from the inner circular region enhances too early and remains enhanced too late.

However, even under these adverse conditions, HYPR still demonstrates the general trends. In the HYPR images the two objects are distinguished with blur introduced at the boundary and the general trends of signal intensity variations are demonstrated with inaccuracies caused by the influence of the two objects on each other.

Finally, Fig. 7 shows the results obtained when simulating an early-filling arterial segment proximal to a stenosis, a later-filling arterial segment distal to the stenosis, and an even later-filling venous vessel segment. The width of each vessel segment is 5 pixels, the length of each arterial segment (proximal and distal to the center of the stenosis) is 10 pixels, and the length of the venous segment is 20 pixels. Noise was added to the input images such that the peak SNR in the series was 25. Twenty profiles were used to construct the weighting image for each timeframe and the composite window width was 5 out of 20 timeframes.

The enhancement of each object is demonstrated by the numbered gamma-variate curves measured from the input images, the HYPR images, and the composite images. It is observed that the composite images have high SNR and high spatial resolution but the waveforms demonstrate temporal blurring, the weighting images have high SNR and provide correct temporal information, but they are

spatially blurred, and the HYPR images have high SNR, high spatial resolution, and high temporal resolution, but the temporal information is blurred spatially within the vessels (due to inherent blur in the weighting images and overlap of vessels in the profiles used to construct the weighting images).

The temporal misrepresentation can be seen by observing the waveforms measured from the HYPR images, in that there is a slight dip in the signal from the proximal arterial segment when the distal arterial segment initially rapidly enhances, and there is a slight premature enhancement of the signals from the distal arterial segment and venous segment due to the ongoing enhancement of the proximal arterial segment. The temporal waveforms obtained from the composite images demonstrate that the temporal averaging effect of the sliding window causes misrepresentation of the rapid initial enhancement of all the vessel segments.

DISCUSSION

Function of Composite and Weighting Images

The HYPR method provides time-resolved images with increased frame update rates relative to what can be achieved using conventional MR imaging methods. It does so by using many sampled profiles to form composite images that demonstrate the spatial locations of objects and then assigning temporal information to the objects by multiplying the composite images by weighting images formed using a very small subset of the sampled profiles. Because the composite images are formed by applying filtered back-projection to a large number of profiles, these images are free of artifacts and have a relatively high SNR. However, because the profiles are acquired at many different times, the composite images contain a time-averaged signal for all of the objects.

The weighting images introduce the temporal information into the time series of HYPR images. Using fewer profiles in the weighting images leads to improvements in the frame update rates. However, overlap of objects in a large percentage of profiles will lead to interference between signals at different locations and inaccuracies in the signal intensities in the HYPR images. In these situations, increasing the number of profiles in the weighting image will reduce the fraction of profiles that include overlapping objects, which will result in a decreased influence from those profiles and more accurate weighting, as shown in Fig. 3. For images containing signal at just a few locations, such as contrast-enhanced MR angiograms, weighting images constructed using as few as 8 to 16 profiles provide relatively accurate results with HYPR reconstruction (19).

If weighting images are not able to adequately assign the temporal information (as shown in Figs. 3, 5), then improving the temporal accuracy of the composite images is beneficial. Using a sliding-window approach allows the composite images to more accurately represent the intensity of the objects as they should appear in each HYPR timeframe. This is a useful method for preventing late-enhancing objects from appearing in composite images used in constructing early timeframes (such as preventing

FIG. 6. This simulation represents three challenges for the HYPR method. First, a circular object is contiguous with an annular object. Second, both objects overlap in every profile. Third, the temporal characteristics are very different—the signal intensity of the control object increases and decreases rapidly, whereas the signal intensity of the annular object increases very slowly. This is an arrangement that is not amenable to the HYPR application. However, it is interesting to note that despite these challenges the HYPR images and measured signal intensity curves still demonstrate the general trends. (Note that the images were cropped to magnify the objects.)

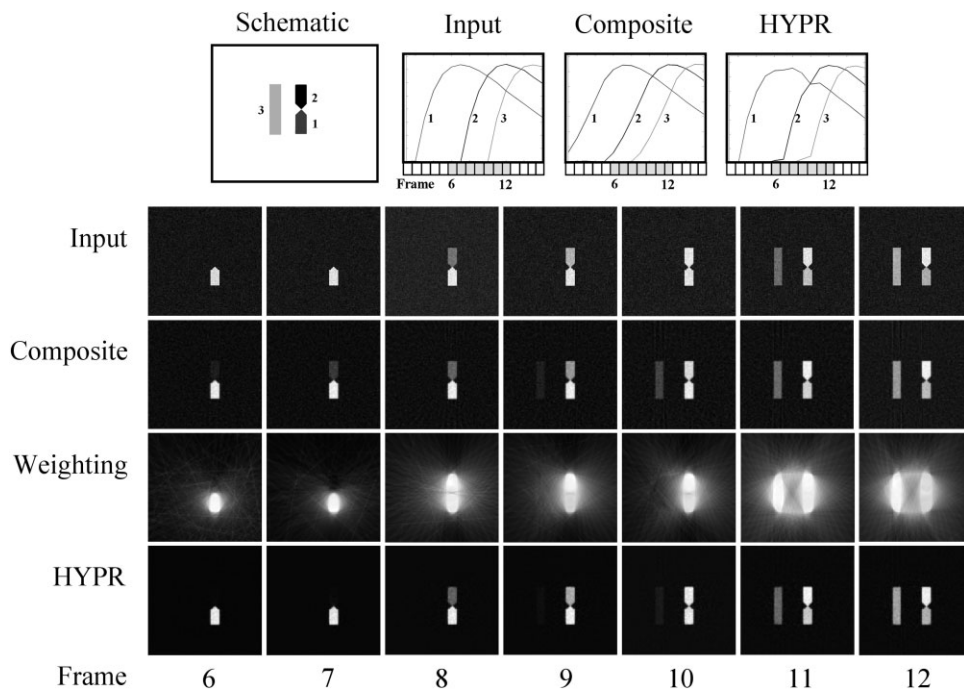
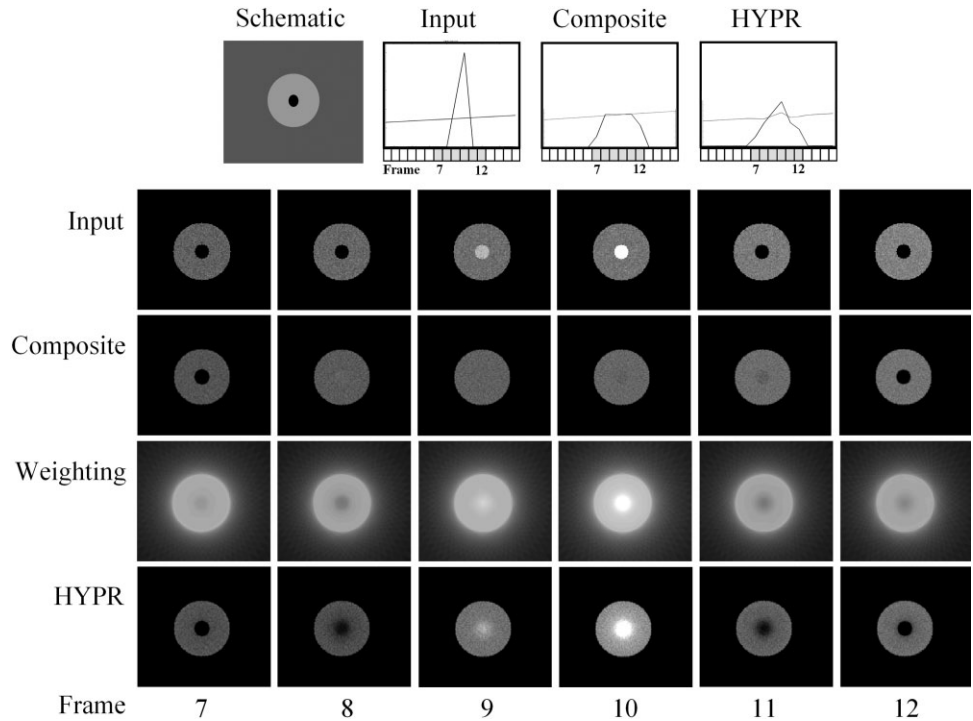


FIG. 7. The enhancement of signal in a vascular stenosis is simulated. A segment proximal to the stenosis (labeled “1” in the schematic) enhances first, followed by enhancement of a segment distal to the stenosis (labeled “2” in the schematic), followed finally by enhancement of an adjacent venous segment (labeled “3” in the schematic). The enhancement of each object is demonstrated by the numbered gamma-variate curves measured from the input images, the HYPR images, and the composite images. The composite images have slightly compromised temporal information, as demonstrated from frames 7 and 10. The weighting images have blurred image quality. The HYPR images combine the advantages of both. By observing the temporal waveforms as measured from the HYPR images, it can be seen that the signal intensity of the three vessel segments slightly influence each other. The images and the time curves demonstrate that the spatial and temporal characteristics of the stenosis are well represented in the HYPR time series, whereas the composite images and associated time curves demonstrate the temporal blurring effect inherent in those images. (Note that the images were cropped to magnify the objects.)

inadvertent enhancement of veins in early arterial images in contrast-enhanced MRA applications). Other methods, such as using a conjugate gradient approach (20) or an iterative HYPR approach (21), have been developed that achieve similar results without relying on reducing the temporal width of the composite images.

Performance of HYPR

In most cases the temporal window width of the HYPR images does not extend beyond that of the weighting images. It is only when the objects are very near each other (as in the upper rows of Figs. 5, 6), or when their signal intensities change dramatically and asynchronously (as in Fig. 6), or when an exceedingly low number of profiles are used in each weighting image (as in the first row of Fig. 3) that some of the temporal information from one object interferes with that of another, degrading the true temporal resolution of the HYPR image series. Under these conditions the temporal window width for some objects extends beyond that of the weighting image, and so for those objects the temporal resolution is not as good as that determined by the frame update rate.

It has been shown that the SNR in a HYPR image is dominated by the SNR in the corresponding composite image (16). Another interesting feature is that the weighting images seem to suppress noise and artifacts in regions outside of signal-generating objects, due to the low weighting values in these regions relative to the weighting values within the objects, and the benefit is greater when fewer objects are present. This leads to a spatially varying noise in the HYPR images. The background signal diminution effect is further enhanced by the zero division protection procedure, which increases the value of P_c (the denominator in the profiles used to produce the weighting images), causing further suppression of low signal information in the HYPR images. It is also possible that the zero protection procedure may lead to diminution of signal from small or low intensity objects if the threshold value is chosen too high, which possibly could be reduced by setting the threshold value based on the SNR of the composite images or weighting profiles.

Sparsity and Spatial-Temporal Correlation

The appearance of HYPR images highly depends on the spatial-temporal conditions of the objects being imaged. A sparse image is one in which the number of signal producing objects is small and the spacing of the objects is large. Sparse images are most amenable to HYPR processing. In sparse images there is a low probability that objects will overlap in the profiles. This allows for a reduced number of profiles to be used in the weighting images (while maintaining accurate temporal information in the HYPR time series) or an improved spatial and temporal accuracy (when a fixed number of profiles are used in the weighting images).

When objects are located closer together the temporal accuracy of the HYPR image series diminishes, as shown in the upper rows of Fig. 5. When objects are closer together it is more likely that they will overlap in one or more projections. This effect can be reduced by using a

larger number of projections in the weighting image in an effort to include more projections that do not contain overlapping objects. Also, when objects are closer together the blurred weighting information from one object will have greater impact on closer neighboring objects and lead to more severe temporal inaccuracies in the HYPR images when the nearby objects appear in the composite images. This effect can be ameliorated by using alternative methods of producing more accurate composite images such as using the sliding window approach or iterative approaches (20,21) or by using alternative filters for generating weighting images that address the trade-off between signal cancellation and spatial blurring.

If the temporal variation of the signal intensities from all the objects is nearly the same, then the accuracy of the HYPR images is relatively independent of the object spacing because it no longer matters that the temporal weighting from one object overlaps another object. Conversely, if the signal intensities of objects change rapidly and the changes are dramatically different for different objects, the temporal averaging effect caused by composite images with large temporal window widths becomes more influential and the interference between different objects becomes more prominent. In these cases, temporal variations are more accurately represented by using more accurate composite images.

The quantitative analyses revealed that the cross-correlation between the input and HYPR curves for each object decreased slightly as the spacing between the objects decreased, or as the temporal variations for each of the objects became more dissimilar. This suggests that the sparsity and spatiotemporal characteristics of a clinical scenario can be used to aid in the selection of imaging parameters to obtain an acceptable level of error in the HYPR image series.

Challenges

As described, closely spaced objects and low temporal correlation are two characteristics that present challenges for the HYPR algorithm. The simulation shown in Fig. 6 demonstrates a worst-case scenario where these two challenges are combined. Nevertheless, even under these conditions where it would be ill-advised to use the HYPR algorithm, it still performs relatively well. Observing the temporal waveforms confirms that the HYPR images demonstrate the temporal variations better than the sliding-window composite images.

Motion is another condition that presents a challenge for the HYPR algorithm. If an object moves during the acquisition, then that object will be blurred in the composite images. The best solution to this issue is to minimize motion. Another solution is to further reduce the composite window width, thereby reducing the time over which motion is allowed to influence the image quality. This, in combination with other approaches, has been used successfully to image the beating heart with HYPR (22).

Clinical Scenario

In clinical applications, acquisitions are in 3D, the frame update rates are dependent on the imaging parameters,

and the temporal variations in signal intensity are dependent on the clinical conditions being evaluated. In order to keep the results general in this study, the simulations were conducted using 2D images, with frame update rates sufficient to provide 20 timeframes during signal evolution. The results can be related to specific applications. For example, when applying a HYPR 3D stack-of-stars acquisition to peripheral MRA, the frame update time is determined by the number of projections used to produce each slice image in a timeframe, the number of slices contained in each timeframe, and the repetition time (TR) of the acquisition sequence. The signal evolution time is determined by the contrast material injection rate and duration and the hemodynamics of the patient. Using a 2D fast multiphase Cartesian acquisition, we have observed (23) the signal intensity changes in the peripheral vessels during the passage of contrast material injected at a rate of 2.0 cc/sec for durations between 10 and 20 sec (as we have been using in our initial applications of HYPR 3D stack-of-stars). The signal intensity rapidly increased and then rapidly or slowly decreased (similar to a gamma-variate function) with the appreciably enhanced signal persisting for 20 to 30 sec, depending on the injection rate and duration. With a HYPR 3D stack-of-stars acquisition having a TR of 4 ms, using 8 projections per timeframe and 32 slices per timeframe, the frame update time is about 1.0 sec, so 20 frames (as simulated) could be sampled during 20 sec of signal enhancement. If 64 slices were acquired the time per frame would be 2 sec and the simulations would be valid if the duration of the contrast material injection were doubled, or if only every second simulated timeframe were considered.

Reconstruction Parameters

With HYPR the appropriate reconstruction parameters are different for different clinical applications and different patients and are determined by the sparsity and spatiotemporal conditions. It is desirable to have flexibility to choose reconstruction values after data are acquired, which demands the use of a special projection acquisition order—like the bit-reversed order, which was used in this study.

If the order of the projections is determined prior to acquisition (by the number of projections per timeframe and composite window width), then when the sequential acquisition order is used as shown in Fig. 1a, reducing the composite window width during reconstruction will lead to an uneven distribution of profiles in the composite image, leaving large gaps in the dataset as indicated by the blank regions in Fig. 1c, and resulting in reconstruction of a poor quality image as shown in Fig. 1e. Thus, with the sequential approach, flexibility to modify parameters during reconstruction is restricted.

In contrast, the bit-reversed projection acquisition order demonstrated in Fig. 1b provides greater flexibility. With the bit-reversed order it is possible to retrospectively choose an arbitrary composite window width and use an incomplete set of profiles without leaving large gaps of missing data. The gaps would be uniformly distributed as shown in Fig. 1d, which results in reconstruction of higher-quality images as shown in Fig. 1f. Furthermore, the

bit-reversed order distributes any changes in signal intensity that occur during acquisition more uniformly over the full set of profiles as demonstrated in Fig. 1b, which leads to a reduction in artifacts caused by angularly dependent signal variations.

If the bit-reversed order is applied to the entire set of projections (rather than to the interleaved sets, within each of which evenly spaced angles are sampled sequentially), then, independent of how many projections are used to reconstruct each timeframe, the projections in each timeframe will be evenly spaced. This allows an arbitrary number of profiles to be used when producing the weighting images, providing flexibility in arbitrarily choosing the frame update rate during reconstruction.

CONCLUSIONS

In this study various simulations were performed to evaluate the behavior of the HYPR reconstruction method under different spatial and temporal conditions. The simulations revealed that the temporal accuracy and quality of HYPR images are typically very good and depend not only on the sparsity and spatial-temporal correlation of images but also on the number of projections used to produce the weighting images, the composite window width, and a host of other parameters. These results are helpful in understanding under what conditions the HYPR method will be the most and least applicable, and how the acquisition and reconstruction parameters should be selected based on these conditions.

REFERENCES

1. Riederer SJ, Tasciyan T, Farzaneh F, Lee JN, Wright RC, Herfkens JR. MR fluoroscopy: technical feasibility. *Magn Reson Med* 1988;8:1–15.
2. Kerr AB, Pauly JM, Hu BS, Li KC, Hardy CJ, Meyer CH, Macovski A, Nishimura DG. Real-time interactive MRI on a conventional scanner. *Magn Reson Med* 1997;38:355–367.
3. Cashen TA, Carr JC, Walker MT, Hopkins JK, Shin W, Carroll TJ. 3D time-resolved contrast-enhanced MRA with sliding subtraction. In: *Proc 14th Annual Meeting ISMRM, Seattle; 2006 (Abstract 570)*.
4. Doyle M, Walsh EG, Blackwell GG, Pohost GM. Block regional interpolation scheme for k-space (BRISK): a rapid cardiac imaging technique. *Magn Reson Med* 1995;33:163–170.
5. Van Vaals JJ, Brummer ME, Dixon WT, Tuithof HH, Engels H, Nelson RC, Gerety BM, Chezmar JL, den Boer JA. “Keyhole” method for accelerating imaging of contrast agent uptake. *J Magn Reson Imaging* 1993; 3:671–675.
6. Korosec FR, Frayne R, Grist TM, Mistretta CA. Time-resolved contrast-enhanced 3D MR angiography. *Magn Reson Med* 1996;36:345–351.
7. Peters DC, Korosec FR, Grist TM, Block WF, Holden JE, Vigen KK, Mistretta CA. Undersampled projection reconstruction applied to MR angiography. *Magn Reson Med* 2000;43:91–101.
8. Vigen KK, Peters DC, Grist TM, Block WF, Mistretta CA. Undersampled projection-reconstruction imaging for time-resolved contrast-enhanced imaging. *Magn Reson Med* 2000;43:170–176.
9. Du J, Carroll TJ, Wagner HJ, Vigen KK, Fain SB, Block WF, Korosec FR, Grist TM, Mistretta CA. Time-resolved, undersampled projection reconstruction imaging for high resolution CE-MRA of the distal runoff vessels. *Magn Reson Med* 2002;48:516–522.
10. Barger AV, Block WF, Toropov Y, Grist TM, Mistretta CA. Time-resolved contrast-enhanced imaging with isotropic resolution and broad coverage using an undersampled 3D projection trajectory. *Magn Reson Med* 2002;48:297–305.
11. Sodickson DK, Manning WJ. Simultaneous acquisition of spatial harmonics (SMASH): fast imaging with radiofrequency coil arrays. *Magn Reson Med* 1997;38:591–603.

12. Pruessmann KP, Weiger M, Scheidegger MB, Boesiger P. SENSE: sensitivity encoding for fast MRI. *Magn Reson Med* 1999;42:952–962.
13. Griswold MA, Jakob PM, Heidemann RM, Nittka M, Jellus V, Wang J, Kiefer B, Haase A. Generalized autocalibrating partially parallel acquisitions (GRAPPA). *Magn Reson Med* 2002;47:1202–1210.
14. Tsao J, Boesiger P, Pruessmann KP. k-t BLAST and k-t SENSE: dynamic MRI with high frame rate exploiting spatiotemporal correlations. *Magn Reson Med* 2003;50:1031–1042.
15. Huang Y, Gurr D, Wright GA. Three-dimensional reconstruction of limited-view projections for contrast-enhanced magnetic resonance angiography at high temporal and spatial resolution. *Magn Reson Med* 2006;55:68–74.
16. Mistretta CA, Wieben O, Velikina J, Block WF, Perry J, Wu Y, Johnson K, Wu Y. Highly constrained backprojection for time-resolved MRI. *Magn Reson Med* 2006;55:30–40.
17. Liang Z-P, Lauterbur PC. An efficient method for dynamic magnetic resonance imaging. *IEEE Trans Med Imaging* 1994;13:677–686.
18. Winkelmann S, Schaeffter T, Koehler T, Eggers H, Doessel O. An optimal radial profile order based on the Golden Ratio for time-resolved MRI. *IEEE Trans Med Imaging* 2007;26:68–76.
19. Wu Y, Wu Y, Korosec FR, Wieben O, Unal O, Du J, Peters D, Mistretta CA. Peripheral angiographic applications of HYPR TRICKS. In: Proc 14th Annual Meeting ISMRM, Seattle; 2006 (Abstract 3644).
20. Griswold M, Barkauskas K, Blaimer M, Moriguchi H, Sunshine J, Duerk J. More optimal HYPR reconstructions using a combination of HYPR and conjugate-gradient minimization. In: Proc 18th Annual Meeting International MRA Club, Basel, Switzerland; 13–15 September 2006, p 29.
21. O'Halloran RL, Holmes J, Fain SB. Iterative reconstruction of time-resolved projection images using highly constrained back projection (HYPR). In: Proc ISMRM Workshop on Non-Cartesian MRI, Sedona, AZ; 25–28 February, 2007.
22. Velikina JV, Wieben O, Mistretta CA, Keith L. An application of HYPR and McKinnon-Bates algorithms to fast cardiac imaging. In: Proc 18th Annual Meeting International MRA Club, Basel, Switzerland; 13–15 September 2006, p 35.
23. Wu Y, Wieben O, Mistretta CA, Korosec FR. 3D HYPR in CE MRA of the lower extremities. In: Proc 15th Annual Meeting ISMRM, Berlin; 2007 (Abstract 1920).